UNIVERSITY OF BIRMINGHAM

Effects of ambient pressure on ignition and flame characteristics in diesel spray combustion

Pang, Kar Mun; Jangi, Mehdi; Bai, Xue Song; Schramm, Jesper; Walther, Jens Honore; Glarborg, Peter

1   **Effects of ambient pressure on ignition and flame characteristics in diesel spray combustion**

2   Kar Mun Pang[a,*], Mehdi Jangi[b], Xue-Song Bai[c], Jesper Schramm[a], Jens Honore Walther[a,d], Peter

3   Glarborg[e]

4   [*]Corresponding author's email: kmpan@mek.dtu.dk

5   [a]Department of Mechanical Engineering, Technical University of Denmark, 2800 Kgs. Lyngby,

6   Denmark

7   [b]Department of Mechanical Engineering, University of Birmingham, B15 2TT Birmingham, UK

8   [c]Department of Energy Sciences, Lund University, 22100 Lund, Sweden

9   [d]Computational Science and Engineering Laboratory, ETH Zürich, CH-8092 Zürich, Switzerland

10   [e]Department of Chemical and Biochemical Engineering, Technical University of Denmark, 2800

11   Kgs. Lyngby, Denmark

12

13   **Abstract**

14   This work reports on numerical investigation of effects of ambient pressure (P_{am}) on spray

15   combustion under engine-like conditions. Three cases with different P_{am} of 42, 85 and 170 bar at

16   a fixed ambient temperature of 1000 K are considered. Zero-dimensional calculations are first

17   performed for autoignition of stagnant adiabatic homogenous mixtures to evaluate performance

18   of the selected diesel surrogate fuel models and to identify the P_{am} effects on the most reactive

19   mixture. An Eulerian-based transported probability density function model is then chosen for the

20   three-dimensional computational fluid dynamics study. The results show the predicted ignition

21   delay times and flame lift-off lengths are in reasonably good agreement with experiment, with the

22   relative difference below 28%. The current work reveals that low-temperature reactions occur

23   across a wide range of mixture fraction but a noticeable rise of temperature (>100 K above

24   ambient temperature) is detected first on the fuel-lean side of the stoichiometric line in all three

25   cases. The high-temperature ignition occurs first on the fuel-rich side in the 42 and 85 bar cases,

26   where the igniting mixture appears to be more fuel-rich in the latter case. As P_{am} is further

27   increased to 170 bar, the igniting mixture becomes more fuel-lean and the high-temperature

28   ignition occurs on the fuel-lean side. The ignition behavior is found to depend on both physical

29   and chemical processes. At 170 bar, the reaction rate increases and the associated transition from

30   low- to high-temperature ignition is relatively fast, as compared to the transport of warmer

31   products from the lean zone into the fuel-rich mixture. Also, within the fuel-rich region, the local

32   temperature is low due to liquid fuel vaporization and the condition is not appropriate for

33   ignition. These collectively cause the high-temperature ignition to occur on the fuel-lean side.

34   Analyses on the quasi-steady spray flame structures reveal that, apart from poorer air entrainment

35   due to reduced lift-off length, the higher rich-zone temperature and lower scalar dissipation rate

36   also lead to a higher peak soot volume fraction at higher P_{am}.

38   **Keywords:** spray flame, transported probability density function, ignition, pressure effects

40   **1. Introduction**

41   Over the last few decades, automotive, light-duty, heavy-duty and marine engine industries have

42   been working on improving the understanding of in-cylinder phenomena, which is an important

43   prerequisite to design clean and efficient engines [1-12]. Numerous research groups, mainly led

44   by the Sandia National Laboratory, share their optical measurements and modelling results

45   through the Engine Combustion Network (ECN) [3], with the aim to facilitate and consolidate

46   diesel spray combustion research. Effects of a wide range of diesel engine parameters on fuel

47   penetration, ignition delay time (IDT), flame lift-off length (LOL) and soot volume fraction

48   ($f_{v,soot}$) have been studied. However, the majority of these studies were performed for an ambient

49   density (ρ_{am}) range of 14.8 to 22.8 kg/m^3. In particular, the Spray A condition, where ρ_{am} is fixed

50   at 22.8 kg/m^3 has been broadly studied in the last couple of years, with an emphasis on

51   understanding the ignition and flame stabilization processes [4-7]. The initial ambient air

52   temperature before the air is cooled by the vaporized fuel, T_{am}, is set to 900 K, corresponding to

an ambient pressure (P_{am}) of ~67 bar. Under the typical range of T_{am} at the start of injection in heavy-duty and large two-stroke marine engines, the ambient densities can be approximately 30.0 and 60.0 kg/m^3 under part and full load conditions, respectively [10,12-15]. Optical accessible experiments conducted at such a high ρ_{am} (or P_{am}) were reported by Siebers and co-workers [8-12]. In their experimental studies, the ρ_{am} was varied from 7.3 to 58.5 kg/m^3, corresponding to a P_{am} of ~20 to ~170 bar at a T_{am} of 1000 K. Under these test conditions, both the liquid and vapor penetration lengths decreased with increasing P_{am}. Besides that, IDT and flame LOL were found to decrease with increasing P_{am}, while the spray flame size at quasi-steady state (in terms of both length and width) reduced when P_{am} increased [10,11]. The effects of P_{am} on ignition and premixed combustion processes up to 45.0 kg/m^3 (~120 bar at T_{am} of 1000 K) were also investigated by Higgins et al. [12]. In terms of soot formation, measurements from optical accessible experiments showed path-length-averaged $f_{v,soot}$ and maximum $f_{v,soot}$ increased with P_{am} [3,13]. Nevertheless, it is challenging to deduce the low- and high-temperature ignition as well as other combustion phenomena solely based on experimental observation at such elevated P_{am}. To date, the effects of P_{am} on spray flame structures under these conditions were not explicitly studied numerically, although these experimental data have been used for computational fluid dynamic (CFD) model validation [16,17]. A more comprehensive understanding of P_{am} effects is crucial for both modelling of engine combustion and for developing physical and chemical models at these P_{am} levels.

Set against this background, the objectives of this CFD work are first to generate velocity, species and temperature distribution profiles to help improving the understanding of the ignition/combustion process at high P_{am} levels; and second to elucidate the effects of P_{am} on spray flame structure and emissions formation. These aims are achieved by employing an Eulerian-based transported probability density function (PDF) method [18] and a skeletal *n*-heptane mechanism [19]. Zero-dimensional calculations are also performed for autoignition of stagnant adiabatic homogenous mixtures to complement the CFD study.

79   The remainder of the paper is structured as follows. In the next section, experimental data

80   used for model validation are first described. It is followed by the descriptions of the numerical

81   methods. The subsequent sections detail the model validation as well as the numerical analyses of

82   autoignition and flame structures at different P_{am} levels. Conclusions from this work are outlined

83   in the final section.

84

85   **2. Experimental data for model validation**

86   The grade number two diesel fuel (diesel #2) spray experimental data used for model validation

87   in this work were obtained in a constant volume pre-burn chamber [9,10]. The initial ambient gas

88   composition is determined by the composition of the combustible-gas mixture burned to generate

89   diesel engine-like temperatures and pressures. In the selected test conditions, the reaction

90    $3.245 \cdot C_2H_2 + 0.515 \cdot H_2 + 8.37 \cdot O_2 + 89.75 \cdot N_2 \rightarrow 89.75\ N_2 + 6.49 \cdot CO_2 + 3.76 \cdot H_2O$ was used to

91   generate the inert high-pressure, high-temperature environment in the non-reacting spray cases. A

92   combustible-gas mixture of 68.1% N_2, 28.4% O_2, 3.0% C_2H_2 and 0.5% H_2 (by volume) was then

93   used in the reacting spray cases. The product composition of this combustible mixture simulated

94   air, having a composition of 21.0% O_2, 69.3% N_2, 6.1% CO_2, and 3.6% H_2O (by volume) [10-

95   12]. The experimental initial ambient gas composition is used in the current reacting spray cases

96   in order to produce identical initial thermochemical conditions. The model performance in

97   simulating fuel penetration lengths of evaporating, non-reacting sprays (cases 1 to 3 shown in

98   Table 1) at different P_{am} is first evaluated. For liquid-phase, the comparison is made against the

99   liquid penetration length determined with the liquid length scaling law. The properties of *n*-

100   heptadecane are used in the liquid length scaling law to produce diesel #2 liquid length [8] since

101   these resemble the properties of diesel #2. The simulated vapor penetration length is compared

102   with the measurements reported by Naber and Siebers [9]. For the validation of the reacting

103   sprays (cases 4 to 6 shown in Table 1), IDT and LOL measurements from the ECN database [3]

104   are used; more descriptions can be found in Ref. [10].

105 Table 1. Operating conditions and injection specifications

Case	$O_{2,am}$	T_{am} [K]	ρ_{am} (kg/m^3)	D_{nozz} (µm)	P_{inj} (bar)	$\dot{m}_f$ (mg/ms)
1	0	1000	13.9	257	1400	14.0
2	0	1000	28.6	257	1400	14.0
3	0	1000	58.6	257	1400	14.0
4[*]	21%	1000	14.8	180	1400	8.8
5[*]	21%	1000	30.0	180	1400	9.0
6[*]	21%	1000	58.5	180	1400	9.2

106 *Note: Non-reacting, vaporising spray simulations are also carried out for cases 4 to 6, where
107 $O_{2,am}$ is set to 0.
108

109   As depicted in Table 1, three cases with different ρ_{am} of 14.8, 30.0 and 58.5 kg/m^3 are

110 considered for the reacting conditions. At a fixed T_{am} of 1000 K, these correspond to P_{am} of 42, 85

111 and 170 bar, respectively. Initial species composition, flow and turbulence conditions can be

112 found in a previous work [20]. The operating conditions as well as the injection specifications

113 including nozzle diameter (D_{nozz}), injection pressure (P_{inj}) and fuel mass flow rate ($\dot{m}_f$) of the test

114 cases are listed in Table 1.

115

116 **3. Numerical methods**

117 3.1 Autoignition of homogeneous mixtures

118 To date, effects of P_{am} on autoignition of various hydrocarbon fuels have been studied in shock

119 tube and plug flow reactor experiments as well as kinetic model simulations. Hashemi *et al.* [21-

120 23] recently studied the effects of P_{am} on C_1-C_3 hydrocarbon reacting pathway up to 100 bar.

121 However, for larger hydrocarbons which are commonly used as diesel #2 surrogate fuels such as

122 *n*-heptane [24,26], *n*-dodecane/myxelene [27] and diesel primary reference fuels [28], the tested

123 P_{am} only considered up to ~50 bar. To the authors' knowledge, validation of diesel #2 surrogate

124 fuel kinetic models for pressure levels of 80 bar and above (targeted conditions in the current test

125 cases) is not available. Thus, five different chemical kinetic mechanisms are evaluated at

126 different P_{am} levels. These include the detailed Lawrence Livermore National Laboratory *n*-

127 heptane model (the Mehl654 mechanism) [24] and two of its skeletal versions (the Liu44 and

128 Lu68 mechanisms) [19,25], a recently updated *n*-heptane model (the Zhang1268 mechanism)

129   [26], and an integrated model of *n*-dodecane and myxelene (the Pei163 mechanism) [27]. To

130   evaluate the selected chemical mechanisms, zero-dimensional (0-D) calculations are conducted

131   for autoignition of stagnant adiabatic homogenous mixtures at three different initial P_{am} of 42, 85

132   and 170 bar using the CHEMKIN-PRO software [29]. The IDT is defined as the time where the

133   mixture temperature increases to 400 K above the initial temperature ($T_{t=0}$). A quadratic relation,

134    $T_{t=0} = T_{am} + 1120Z^2 - 1370Z$, is used to correlate the temperature and mixture fraction. Here, Z is the

135   Bilger mixture fraction while T_{am} is the initial ambient temperature in the combustion chamber

136   and is set to 1000 K. This relation is obtained by post-processing the 3D-CFD results of the

137   reacting case prior to the start of low-temperature ignition, corresponding to the mixing between

138   the cold fuel and hot air. The quadratic relation is constructed for $0 \leq Z \leq 0.4$ and the same

139   function is found applicable to represent the mixing at all three P_{am} (*cf.* Figs. 7 to 9) such that P_{am}

140   is the only variable in the comparison. Akin to that in Ref. [30], the most reactive mixture (Z_{mr}) is

141   characterized as the mixture which has the shortest IDT, and the associated IDT can serve as a

142   reference for the comparison against the results from inhomogeneous and turbulent mixtures [30].

143   It may be worth mentioning that effects of pressure on Z_{mr} have not yet been explicitly studied for

144   turbulent non-premixed flames [31]. Based on the results of Fig. 1, all the models produce similar

145   qualitative trends with respect to the change of P_{am}, *i.e.*, the Z_{mr} occurs in more fuel-lean mixture

146   and Z_{mr} falls closer to the stoichiometric mixture fraction, Z_{st} when P_{am} increases (*cf.* Fig. 1). The

147   results also show that the IDT predicted by the Liu44 mechanism is close to those of its detailed

148   counterpart, in particular near the Z_{mr} regimes. This trend is similar to that reported by Pei et al.

149   [32] under a similar ambient, thermochemical condition, although the fuel temperature is lower at
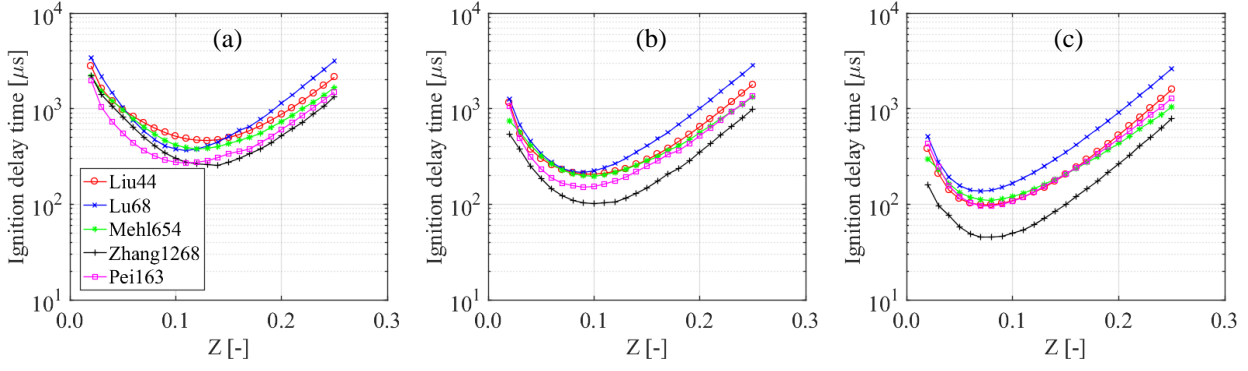
150   373 K in their cases.

151

Fig. 1. Ignition delay times of homogenous mixtures for varying initial mixture fraction and temperatures at (a) 42 bar, (b) 85 bar and (c) 170 bar.
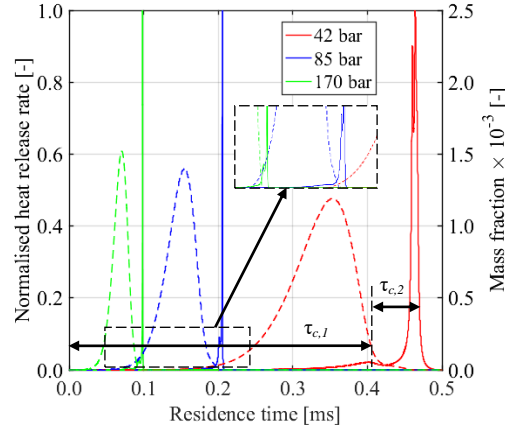

Fig. 2. Ignition histories of Z_{mr} computed in the zero-dimensional homogenous reactor model using the Liu44 mechanism. Solid lines denote the normalized heat release rate while dotted lines represent the mass fraction of RO_2.

In the case where the Liu44 model is used, Z_{mr} are recorded to be 0.13, 0.10 and 0.07 in 42, 85 and 170 bar case, respectively. The corresponding $T_{t=0}$ are 841 K, 874 K and 910 K, respectively. The simulated heat-release rate (HRR) profiles are plotted in Fig. 2. Temporal evolution of the heptyl radical (RO_2) of these cases are also provided to indicate the low-temperature ignition. Here, the IDTs coincide at the peaks of the HRR. The IDT can be expressed as IDT $= \tau_{c,1} + \tau_{c,2}$, where $\tau_{c,1}$ and $\tau_{c,2}$ are the first-stage (low-temperature) and second-stage (high-temperature) IDTs respectively. All the mixtures in these cases undergo two-stage ignition, where

168 the high-temperature ignition occurs after the high amount of RO_2 is consumed. It is also noted in

169 the insets of Fig. 2 that $\tau_{c,2}$ becomes negligible when the P_{am} increases. The Liu44 mechanism is

170 therefore chosen for the 3-D CFD simulations, which are described next.

171

172 3.2 CFD model formulation

173 The 3-D CFD spray combustion simulations are carried out using OpenFOAM version 3.0.1 [33].

174 Detailed descriptions of the model can be found in [35] and only a brief description is provided

175 here. The fuel spray, flow and combustion processes are modelled using the Eulerian-Lagrangian

176 approach within the unsteady Reynolds averaged Navier-Stokes (URANS) framework. The

177 Reitz-Diwakar model is used to simulate the fuel droplet breakup, while the Realizable $k-\varepsilon$

178 model is employed for turbulence modelling. For the nitric oxide (NO) formation modelling, the

179 Zeldovich thermal NO sub-mechanism from Ref. [34] are added to the Liu44 mechanism. The

180 interaction between turbulence and chemistry is modelled using the Eulerian-based transported

181 PDF method, Eulerian Stochastic Field (ESF) [18]. Similar to the Lagrangian particle transported

182 PDF method, the ESF method is a general approach to account for the turbulence-chemistry

183 interaction (TCI). It can be used to simulate the autoignition as well as different levels of

184 'premixedness' $i.e.$, premixed, partially premixed and non-premixed. In the ESF method, the

185 governing equation for the n-th stochastic field is

186
$$
\bar{\rho}d\phi_a^{(n)} = -\bar{\rho}\tilde{u}_i \frac{\partial\phi_\alpha^{(n)}}{\partial x_i}dt + \bar{\rho}S_\alpha^{\ r}(\phi^{(n)})dt + \bar{\rho}S_\alpha^{\ s}(\phi^{(n)})dt
$$
$$
+ \frac{\partial}{\partial x_i}\left(\Gamma_t \frac{\partial\phi_\alpha^{(n)}}{\partial x_i}\right)dt - \frac{1}{2}\bar{\rho}C_\phi(\phi_\alpha^{(n)} - \tilde{\phi}_\alpha)\omega_t dt + \bar{\rho}\sqrt{2\frac{\Gamma_t}{\bar{\rho}}}\left(\frac{\partial\phi_\alpha^{(n)}}{\partial x_i}\right)dW_i^{(n)}
$$
(1)

187 where ϕ_a denotes the mass fraction of species (Y_i) or the enthalpy of the mixture (h), and

188 $\phi^{(n)} = \left[Y_1^{(n)}, Y_2^{(n)}, ... Y_i^{(n)}, h^{(n)}\right]$. The first term on the right hand side (r.h.s.) represents the

189 convective term while the second term, $\bar{\rho}S_\alpha^{\ r}(\phi^{(n)})dt$, is due to the chemical reactions. The third

190 term, $\bar{\rho}S_\alpha^{\ s}(\phi^{(n)})dt$, is the source term due to the spray evaporation. This is different for each

191 species, $i.e.,$ solely the evaporating species is involved but it is identical for each stochastic field.

8

The fourth term corresponds to a gradient transport model for turbulent velocity fluctuation, where $\Gamma_t = \mu_t / \sigma_t$ is the turbulent diffusivity. Here, μ_t is the turbulent viscosity while σ_t is the turbulent Schmidt number (Sc_t) in the transport equations for chemical species or the Prandtl number (Pr_t) in the enthalpy transport equation. Both Sc_t and Pr_t are set to 0.7 in the current work. The fifth term, which involves the mixing constant, C_ϕ, represents the molecular mixing. The mixing constant is fixed at $C_\phi = 2$. It is modelled using the Interaction with Exchange to the Mean model. ω_t therein is the turbulence frequency obtained from $\omega_t = \varepsilon / k$ where k and ε are the turbulent kinetic energy and its dissipation rate, respectively. In the last term on the r.h.s., $dW^{(n)}$ represents a vector Wiener process that is spatially uniform but different for each field. The purpose of this term is to introduce a stochastic noise in the transport equations and generate consequent PDF for chemical species and enthalpy. In these simulations, $dW^{(n)}$ is represented by a time-step increment $\Delta t^{1/2} \eta_i^n$, where $\eta_i^n = \{-1,1\}$ is a dischotomic random vector. Previous work has shown that the use of thirty-two stochastic fields reached result convergence [35]. The Chemistry Coordinate Mapping (CCM) approach is coupled with the ESF solver in order to integrate the chemical reaction source terms efficiently [36]. In the current work, a four-dimensional phase space based on temperature, local equivalence ratio, scalar dissipation rate, and the mass fraction of fuel is used. Their resolutions are fixed at 5 K, 0.01, 0.025 and 0.001 respectively. The ESF-CCM solver is incorporated with a revised multi-step soot model [14,20]. Mean molar concentrations of acetylene (C_2H_2) and O_2/OH are used to estimate the soot formation and oxidation rates respectively. Both soot and gas radiation heat transfers are not considered in the current work. Bolla et al. [37] showed that the effect of radiation heat transfer influences the local flame temperature in the order of O(10 K) and hence has minor influence on local NO and soot concentrations under the Spray A condition. While the effects of radiation heat transfer are more significant at higher P_{am} due to the increased concentrations of soot, CO_2 and H_2O, they may only vary the absolute values. Comparisons to the experimental results in section

217 4 show variation of combustion and emissions characteristics with respect to the change of P_{am}

218 levels are captured by the current model. These qualitative trends are expected to remain

219 unchanged with the consideration of radiation heat transfer.

220 The computational domain is a constant volume chamber, which has a cubic shape with

221 side lengths of 108 mm. The injector is placed at the center of one of the chamber walls. A

222 uniform Cartesian grid is used. In the previous study, an isotropic cell size of 0.5 mm within the

223 spray combustion region was found to reach mesh independence [35]. This mesh resolution is set

224 as the baseline configuration and mesh sensitivity studies are carried out for different P_{am} in the

225 current work. The computational grid with the fine, intermediate (baseline) and coarse resolutions

226 consists of approximately 1,440,000, 360,000 and 89,000 cells, respectively. Figure 3 shows that

227 the penetration lengths and mixture fraction generated by the finer resolution and the baseline are

228 close while those by the coarser resolution deviate, particularly for liquid fuel penetration length.

229 It should also be mentioned that the qualitative change of the ignition behavior (see Section 4)

230 with respect to the variation of P_{am} is also consistent when a finer resolution is used.

231
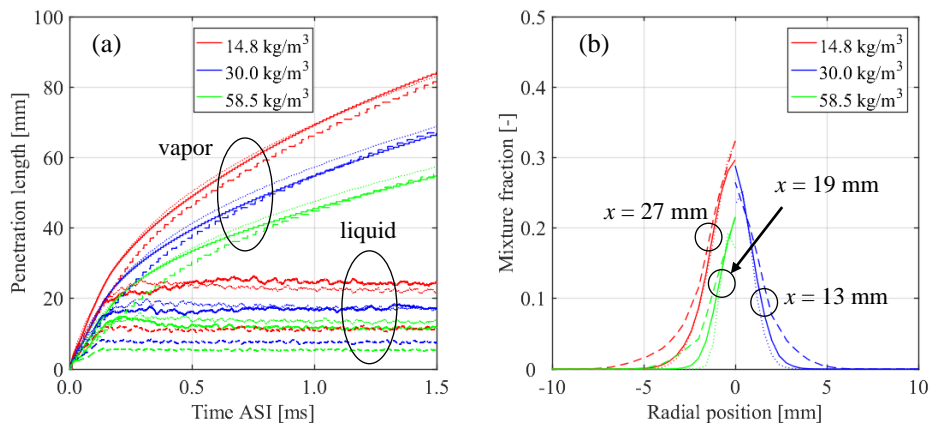
232

233 Fig 3.(a) Penetration lengths and (b) mixture fraction distribution at axial position (*x*) near the

234 end of liquid penetration length predicted using different mesh resolution. Dashed-, solid- and

235 dotted-lines are results of the coarse, intermediate (baseline) and fine resolutions, respectively.

236

237

4. Results and discussion

4.1 Model validation

Figure 4 depicts the temporal evolution of the liquid and vapor penetration lengths of the evaporating, non-reacting sprays from the experiments and the numerical models. The liquid penetration reaches steady state after 0.5 ms, while the vapor penetration continues to grow with time. The model is capable to replicate the experimental penetration lengths reasonably well. As the P_{am} increases and hence the ρ_{am} increases, both the liquid and vapor penetration lengths decrease due to the increased droplet drag caused by the higher ρ_{am}.
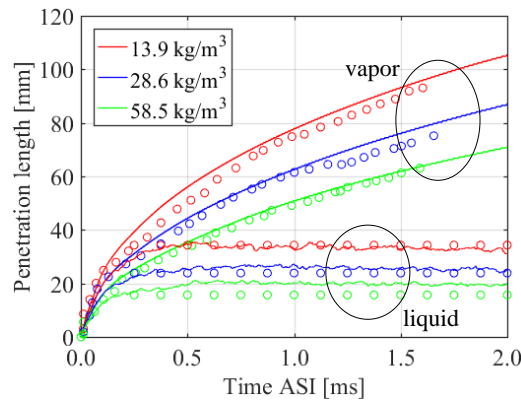

Fig. 4. Liquid and vapor penetration lengths of the evaporating, non-reacting sprays (cases 1 to 3) as a function of time after start of injection (ASI). Solid lines denote the simulation results while markers are obtained by liquid scaling law (liquid) [8] and from the experiment (vapor) [9].

Model evaluation is performed further for evaporating, non-reacting sprays with D_{nozz} of 180 µm. Since experimental data are not available for D_{nozz} of 180 µm, model evaluation is carried out based on liquid scaling law [8] as well as dimensionless penetration length and time [9]. The current spray breakup model configuration is found applicable for both D_{nozz} of 180 and 257 µm, *i.e.*, the same spray sub-model constants were used. Figure 5 shows that the predicted liquid penetration length of the non-reacting sprays for D_{nozz} of 180 µm (cases 4 to 6 with $O_{2,am} = 0\%$) agree with the liquid scaling law [4]. The associated vapor penetration length is evaluated using the dimensionless spray tip penetration distance (σ) and dimensionless penetration time (τ).

11

As seen in Fig. 5, all the σ curves collapse, agreeing well with the trend reported in [5]. This indicates that the dependence of vapor penetration length on ρ_{am} is successfully simulated by the model.

Fig. 5. Predictions of liquid penetration lengths and dimensionless penetration distance (σ) as a function of dimensionless penetration time (τ). Circle markers denote liquid scaling law results.

Fig. 6. Flame lift-off positions of the reacting sprays (cases 4 to 6) as a function of time after start of injection (ASI). Vertical and horizontal dash-dotted lines with asterisks represent the experimental ignition delay times and averaged flame liftoff lengths respectively [3,10]. Magenta dotted line indicates the boundary separating the domain of ignition (larger time ASI) and induction to ignition (smaller time ASI).

The decrease in both liquid and vapor penetration lengths lead to the ignition site and the flame stabilization position to move upstream towards the injection tip, reducing the LOL (see
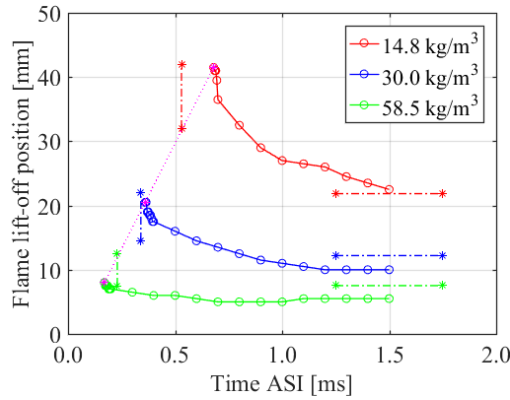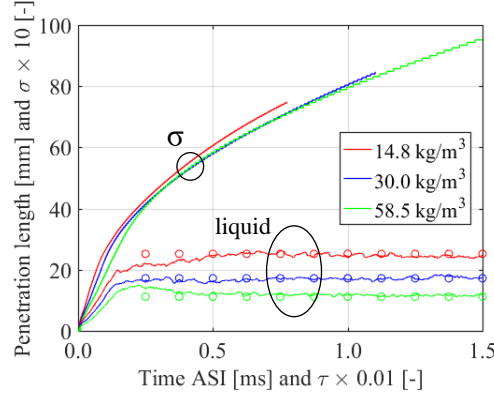
12

277 Fig. 6). A comparison to the measurements shows that the IDTs and flame LOLs are predicted

278 within 28% for all three cases. The difference is mainly attributed to the overestimated IDT in the

279 42 bar case. It is interesting to note that a similar simulation result was reported by Bolla et al.

280 [17], when a different TCI closure approach, the conditional moment closure model, was

281 employed with the same mechanism for the same thermochemical conditions. Although the IDTs

282 and LOLs predicted are to a certain extent different from the experiment, the trend of IDT and

283 LOL with respect to the change of P_{am} is correctly predicted.

284

285 4.2 Autoignition characteristics of diesel spray combustion

286 Figures 7 to 9 illustrate the autoignition characteristics of the three cases using scatter plots of

287 temperature (T)-mixture fraction (Z) and contours of various combustion products. In the 42 bar

288 case, RO_2 is formed in the fuel-rich inner core of the spray jet with a temperature around 750 K,

289 starting at approximately 350 µs (not shown). Through the low-temperature reaction pathway,

290 RO_2 oxidizes to ketohydroperoxide. The HO_2 radical is formed in the vicinity of

291 ketohydroperoxide, extending to the fuel-lean side of the stoichiometric line. These species are

292 formed downstream of the liquid fuel. The first-stage ignition is found across a wide range of

293 mixture fraction. As shown in Fig. 7(a), a small amount of OH is formed at 670 µs on the fuel-

294 lean side and the peak temperature increases above 1100 K. Figure 7(b) depicts that HO_2 reaches

295 a higher concentration in the fuel-rich zone at 695 µs, as compared to that in the fuel-lean zone.

296 HO_2 in this region is first consumed and OH is formed. The local temperature increases beyond

297 the temperature threshold of 1400 K (400 K above T_{am}), indicating the onset of the main ignition.

298 Rate of production (ROP) analysis of the 0-D simulation of Z_{mr} (in section 4.1) shows that OH is

299 mainly formed from the sequence $HO_2+HO_2 \leftrightarrow H_2O_2+O_2$ (R1), $H_2O_2+M \leftrightarrow 2OH+M$ (R2), where M

300 is the third body species. It is also noticed that the main ignition occurs in the region where the

301 scalar dissipation rate (χ) is low and the residence time is long (within the center of the

302 recirculation zone).

13

303
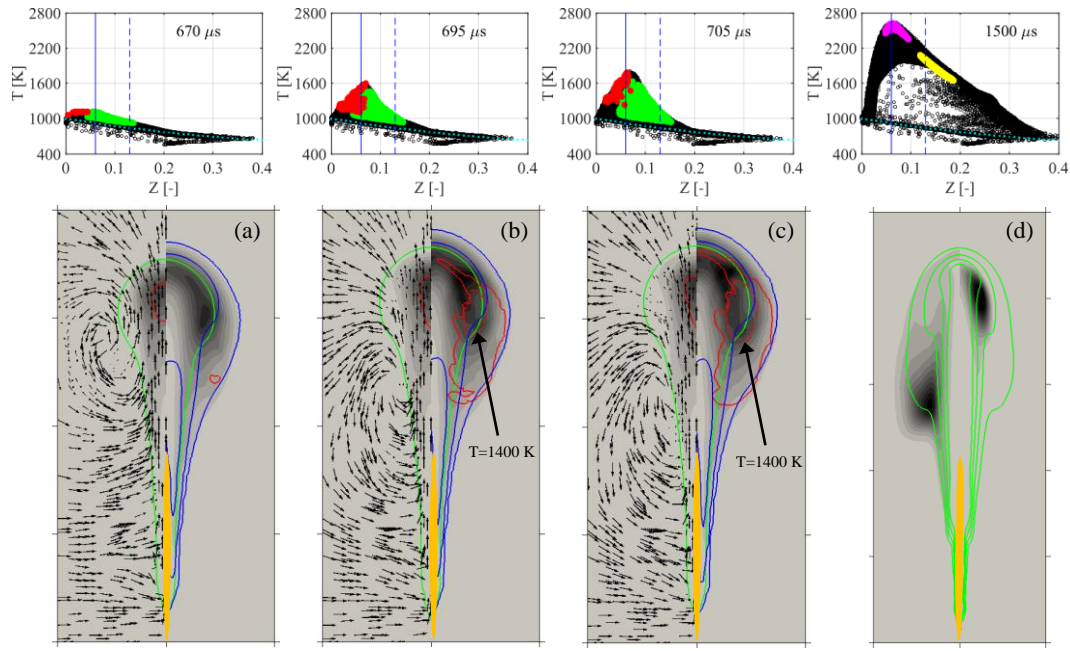
Fig. 7. Scatter plots of temperature-mixture fraction (upper row) and contours of combustion

products (bottom row) in the 14.8 kg/m^3 case a) at first-stage ignition, b) at onset of second-stage

ignition, c) towards the formation of a classical diesel spray flame and d) during quasi-steady

state. Upper row: Cells with substantial formation of HO$_2$, OH, NO and soot volume fraction

($f_{v,soot}$) are marked with green, red, magenta and yellow respectively. The thresholds are set to

40% of their respective maximum mass fraction. Stoichiometric lines, the most reactive mixture

fraction and mixing lines are represented by solid blue, dashed blue and dotted cyan lines

respectively. Bottom row (a)-(c): (Left) Ketohydroperoxide contour with flowfield (black

arrows), RO$_2$ of 1 x 10^{-4} (solid red); and (right) HO$_2$ contour with isolines of scalar dissipation

rates of 1, 10 and 100 (solid blue), OH mass fraction of 1 x 10^{-4} (solid red), temperature of 1400

K (dotted red); (d) (Left) NO and (right) $f_{v,soot}$ contours at quasi-steady state with isolines of local

equivalence ratio of 1 to 4 (solid green). Maximum mass fraction of ketohydroperoxide, HO$_2$, and

NO is fixed at 0.03, 0.001 and 0.002 respectively while maximum soot volume fraction is set to 5

ppm. Solid green lines indicate the stoichiometric line and the orange lines represent the averaged

liquid length. For (a) to (c), each frame shows 30 x 60 mm while for (d), the frame shows 40 x

100 mm.

320

14

321   The formation of RO_2, ketohydroperoxide and HO_2 starts earlier at approximately 200 µs

322   in the 85 bar case (not shown). Figure 8(a) depicts that OH formation is formed at 350 µs in the

323   fuel-lean region where the local temperature exceeds 1100 K. The second-stage ignition then

324   takes place at 365 µs on the fuel-rich side of the stoichiometric line, in the region where χ is low

325   and the residence time is long. These phenomena are akin to those of 42 bar case discussed

326   above, although the transition from low- to high-temperature ignition has a shorter duration. A

327   shorter transition is also observed in the homogenous reactor calculation (*cf.* Fig. 2). Reaction

328   path analysis shows that reaction R2 remains the most significant step during the main ignition

329   event. When P_{am} increases, the separation between the end of liquid fuel and key radicals such as

330   RO_2, ketohydroperoxide and HO_2 reduces. The ignition site is closer to the penetration tip where

331   the local Z value is higher. In the 42 and 85 bar cases, the mixture on the fuel-lean side first

332   experiences a higher temperature rise, presumably due to the higher T_{am}. It then promotes the

333   low-temperature reactions in the rich mixture due to the transport of warmer lean products into

334   the fuel-rich zone. These phenomena are similar to those reported in Refs. [4-7], which studied

335   the ignition behavior for the Spray A condition ($O_{2,am} = 15\%$; $T_{am} = 900K$; $P_{am} = 60$ bar). The

336   observation that the main ignition event occurs in more fuel-rich mixtures in the case with higher

337   P_{am} is consistent with the findings of Higgins et al. [12] who experimentally studied the ignition

338   behavior at different ρ_{am} in the same combustion vessel. However, the behavior changes when

339   P_{am} is further increased. As discussed next, the current results show that the mixture fraction of

340   the first igniting mixture during the high-temperature ignition does not vary monotonically with

341   P_{am} and the second-stage ignition takes place in a more fuel-lean region in the 170 bar case.
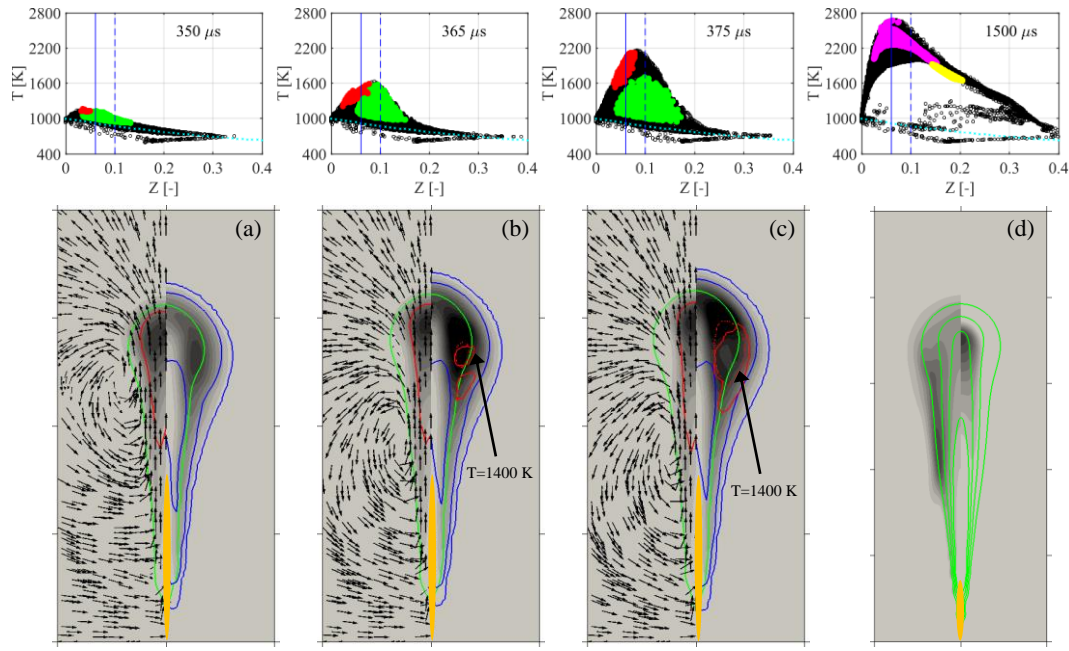
342

Fig. 8. Scatter plots of temperature-mixture fraction (upper row) and contours of combustion products (bottom row) in the 30.0 kg/m^3 case at different times. Descriptions can be found in the caption of Fig. 7, apart from maximum soot volume fraction which is set to 50 ppm. For (a) to (c), each frame shows 20 x 40 mm while for (d), the frame shows 40 x 100 mm.

At 170 bar, RO$_2$, ketohydroperoxide and HO$_2$ are formed early at 100 µs (not shown). The temperature of the fuel-lean mixture increases to above 1100 K at 150 µs. Under this condition, the transition from low- to high-temperature ignition is even faster, occurring in less than 15 µs. The transport of warmer products from the fuel-lean zone into the fuel-rich mixture is relatively slow, as compared to the increased reaction rate. Figure 9 depicts that there is no separation in the spray direction between HO$_2$ and liquid fuel, *i.e.*, HO$_2$ is formed in the vicinity of the fuel spray region. Within the fuel-rich region, the local temperature is low due to evaporation and the condition is not appropriate for ignition. The scatter plots in Figs. 8(b) and 9(b) support that, during the high-temperature ignition, the local temperature within the fuel-rich region becomes lower when P_{am} increases. Eventually, the high-temperature ignition occurs on the fuel-lean side of the stoichiometric line.
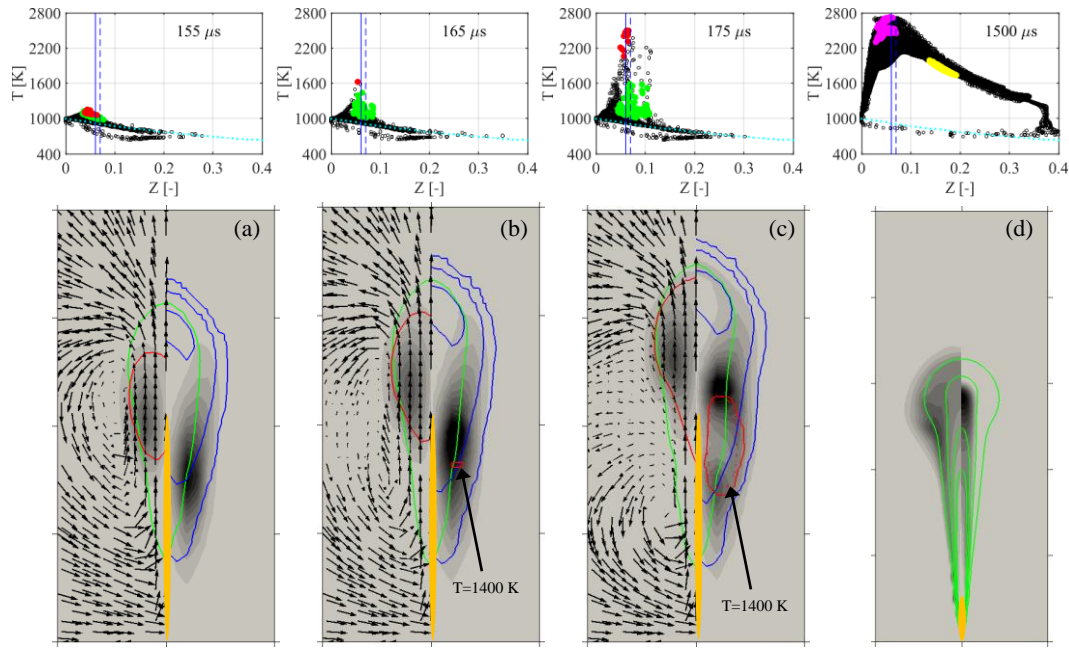
Fig. 9. Scatter plots of temperature-mixture fraction (upper row) and contours of combustion products (bottom row) in the 58.5 kg/m³ case at different times. Descriptions can be found in the caption of Fig. 3, apart from maximum soot volume fraction which is set to 500 ppm. For (a) to (c), each frame shows 5 x 20 mm while for (d), the frame shows 40 x 100 mm.

The ignition characteristics from low- to high-temperature ignition in the three cases are also illustrated using the scatter plots of rate of fuel concentration change and mixture fraction. These plots can be found in Fig. 10. A positive value indicates the presence of vapor fuel while a negative value denotes the fuel consumption. Each plot is colored by the normalized local temperature at that particular timestep, *i.e.*, dark blue, blue, green and yellow represent low, intermediate, high, the highest temperature, respectively. At 42 and 85 bar, the higher temperature regime first falls on the fuel-lean mixture and then shifts to the fuel-rich mixture. During the main ignition process, the fuel has been consumed where the main ignition event occurs. On the other hand, at 170 bar, the vapor fuel is still observed but the corresponding mixture is cold and does not get involved in the ignition process. The mixture on the fuel-lean side of the stoichiometric line undergoes low- and then high-temperature ignition. These support the discussion earlier based on Figs 7 to 9.

17
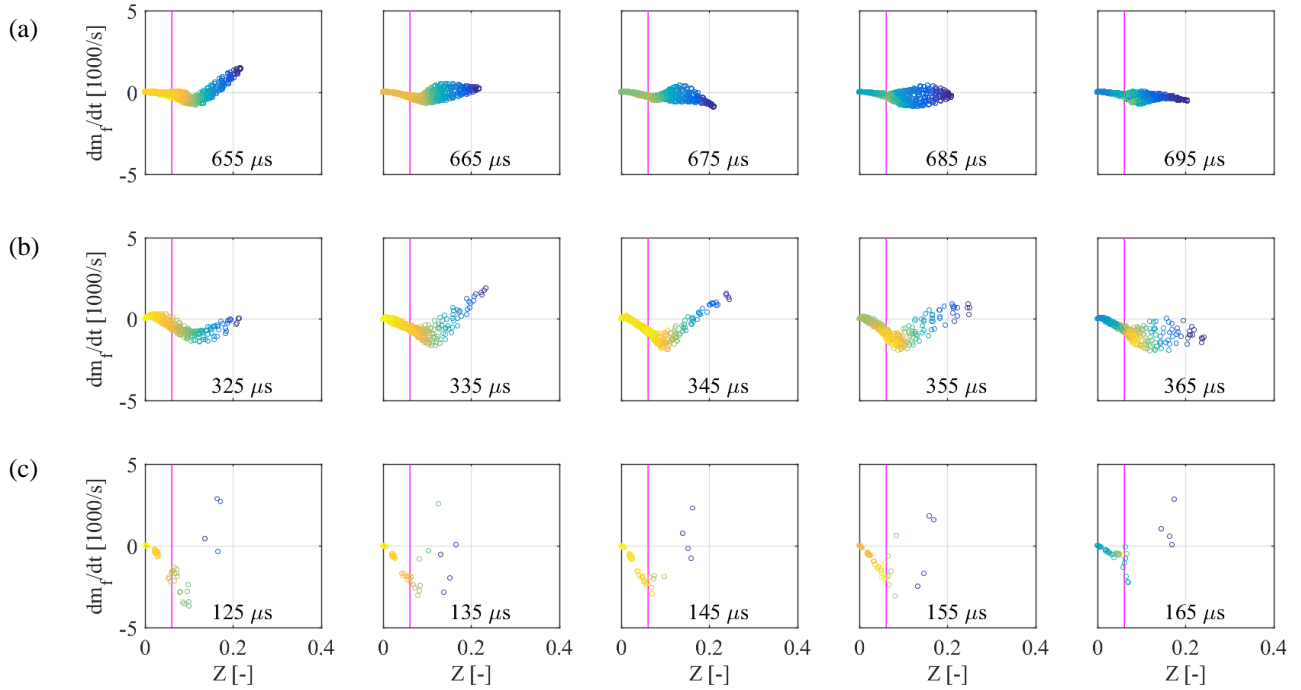
Fig. 10. Scatter plots of rate of fuel concentration change and mixture fraction for (a) the 14.8 kg/m^3 case at 44 mm from the injector tip, (b) the 30.0 kg/m^3 case at 26 mm from the injector tip and (c) the 58.5 kg/m^3 case at 8 mm from the injector tip. The last column provides scatter plots at their respective main high temperature ignition.
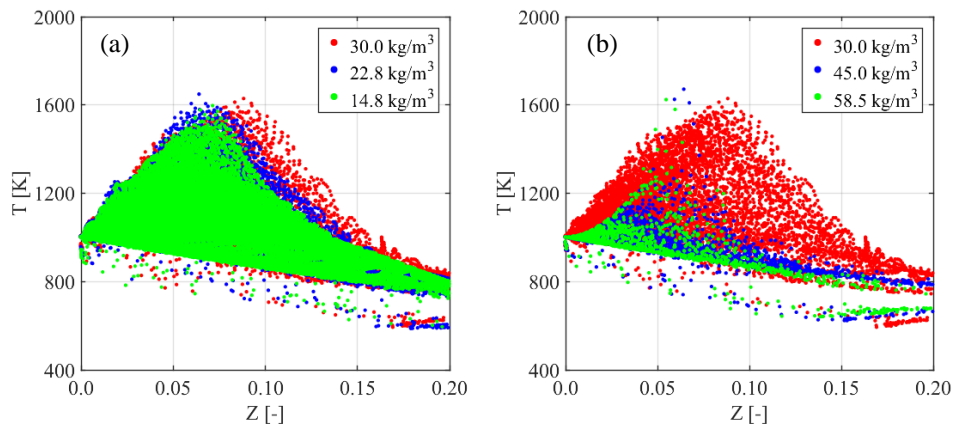
Fig. 11. Scatter plots of temperature-mixture fraction of (a) the 14.8 kg/m^3 case at 695 µs, the 22.8 kg/m^3 case at 470 µs, the 30.0 kg/m^3 case at 365 µs and (b) the 30.0 kg/m^3 case at 365 µs, the 45.0 kg/m^3 case at 230 µs and the 58.5 kg/m^3 case at 165 µs.

391 Computation of two additional intermediate cases of ρ_{am} of 22.8 kg/m^3 (67 bar) and 45.0

392 kg/m^3 (128 bar) confirms this trend. Figure 11 demonstrates that the main ignition occurs in more

393 fuel-rich mixtures when P_{am} increases from 42 bar to 85 bar, consistent with results of Higgins et

394 al. [12]. Above 85 bar, the mixture that undergoes the main ignition becomes more fuel-lean

395 when P_{am} increases. In order to further verify this trend, simulations are performed using the

396 Lu68 mechanism [16] for cases 5 and 6. The predicted IDT using the Lu68 mechanism is slightly

397 closer to the measurement in the 170 bar case (case 6), with a relative difference of < 8% from

398 the measurement, as compared to that using the Liu44 mechanism with a relative difference of

399 ~10% from the measurement. The high-temperature ignition occurs on the fuel-rich side (Z of

400 0.109) and the fuel-lean side (Z of 0.0603) in the 85 bar (case 5) and 170 bar (case 6)

401 respectively, showing that the qualitative change of the ignition behavior with respect to the

402 variation of P_{am} from 85 bar to 170 bar is the same for the Liu44 and Lu68 mechanisms. It should

403 be noted that the variation of Z of the first ignition mixtures during the high-temperature ignition

404 is identified for these particular injection specifications, initial ambient gas composition and T_{am}.

405 As the ignition behavior is dependent of both physical and chemical processes, the variation of Z

406 of the first ignition mixtures during the high-temperature ignition with respect to P_{am} may

407 change. Understanding the ignition behavior is crucial for development of skeletal surrogate fuel

408 mechanisms. Once the ignition behavior is identified for a narrower range of operating

409 conditions, the size of the skeletal surrogate fuel mechanisms can be further optimized to increase

410 the computational efficiency.

411 Effects of P_{am} on the quasi-steady state flame structures will be discussed next. Upon the

412 ignition point, it takes approximately 160 hours for 0.1 ms on ten 64-bit Intel Ivy Bridge Xeon

413 E5-2650 v2 8-core CPUs running at 2.60 GHz with the Liu44 mechanism. The computational

414 cost is expected to escalate significantly with the use of the Lu68 mechanism. Hence, only the

415 Liu44 mechanism is used for the simulations up to quasi-steady state and the associated results

416 are used for the flame structure analyses.

417   4.3 Quasi-steady state
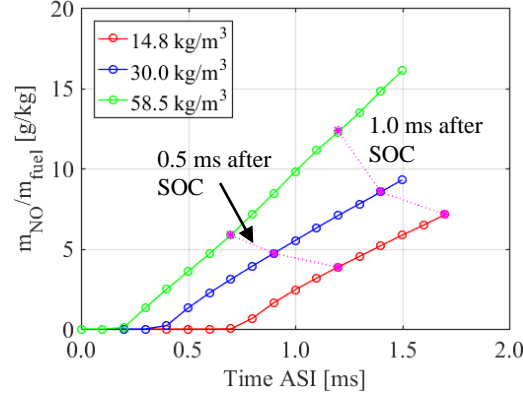
418

419   Fig. 12. Normalized total mass of NO as a function of time after start of injection (ASI). Magenta

420   dotted lines indicate the total NO mass production remains higher after their respective start of

421   combustion (SOC).

422   An analysis based on transport budgets [38] near the lift-off position at quasi-steady state

423   suggests the flame is stabilized by the auto-ignition process. This remains unchanged for three

424   P_{am} levels and agrees with the findings from the literature. In addition to that, the Takeno's flame

425   index (FI) is used to investigate the spray flame structure.   The local equivalence ratio is

426   incorporated into FI such that the premixed flame can be identified for both fuel-lean and fuel-

427   rich conditions, as shown in Eq. (2),

428    $$FI = \frac{\nabla Y_F \cdot \nabla Y_O}{|\nabla Y_F \cdot \nabla Y_O|} \cdot \frac{\phi - 1}{|\phi - 1|}$$ (2)

429   where the mass fraction of fuel, Y_F includes those of evaporating species, n-heptane as well as the

430   main fuel-rich combustion products, $i.e.$ CO and H_2 [35]. The quasi-steady spray structures are

431   found independent from the effects of P_{am} at the tested initial T_{am} and ambient gas composition.

432   Takeno's FI shows that all the spray flames have the classical structure of the diesel spray flames

433   described in the Dec conceptual model, $i.e.$, a premixed rich flame upstream embedded by a

434   diffusion flame which extends downstream [40]. Figures 7(d), 8(d) and 9(d) demonstrate that the

435   location of NO and soot formation regions for the three P_{am} levels. High NO concentration is

436   found above 2200 K near the stoichiometric mixture, while high soot concentration is in the

437   premixed fuel-rich zone with local temperature ranging from 1600 to 2200 K; this result is

20

438 consistent with the literature [40,41]. A decrease in the flame size (in terms of both flame length

439 and width) with the increase of P_{am}, can also be seen in Figs. 7(d), 8(d) and 9(d). An evaluation

440 of the reaction zone thickness based on the full-width at half maximum of OH mass fraction at

441 the middle of the spray flames shows that the thickness of the reaction zone is approximately 7.2,

442 3.2 and 1.6 mm for the 14.8, 30.0 and 58.5 kg/m^3 cases, respectively. These trends are in

443 qualitative agreement with the experimental images based on OH chemiluminescence [11]. The

444 reaction zone thickness for the O radicals exhibits a similar trend as those of OH. The spatial NO

445 distribution becomes narrower when P_{am} increases. Although the reaction zone size decreases

446 with the increasing ambient pressure, the rate of NO formation increases more rapidly with

447 increasing P_{am}. The increased reaction rate attributed by the increased P_{am} is more influential to

448 the final NO production. The total NO formation hence increases with P_{am}, as indicated by the

449 magenta dotted lines in Fig. 12. The current model predicts that the peak soot volume fraction

450 ($f_{v,soot}$) increases approximately six-fold when P_{am} increases from 42 to 85 bar and further

451 increases approximately thirteen-fold when P_{am} further increases from 85 to 170 bar. To date, the

452 revised multi-step model has only been evaluated using $f_{v,soot}$ measurements collected at 42 and

453 85 bar [14,20] since $f_{v,soot}$ measurement above 85 bar is not available. Further work is thus

454 required to confirm the estimation of $f_{v,soot}$ at 170 bar. Yet, the trend of maximum $f_{v,soot}$ increasing

455 with P_{am} agrees with experimental observations [13].

456 Figure 2 shown earlier illustrates that the ignition site is placed further upstream and the

457 flame stabilizes more quickly when P_{am} increases. At quasi-steady state, the flame LOL reduces

458 with increasing P_{am}. This reduces the air entrainment, giving rise to a higher mixture fraction

459 within the fuel-rich core region. Besides that, the elevated reaction rate at higher P_{am} also

460 promotes soot formation. These factors are known to increase the local peak $f_{v,soot}$ [13]. The

461 current study shows that the rise of the soot formation rates can be attributed to other factors. As

462 aforementioned, the flame width reduces for a higher P_{am}. Consequently, the stoichiometric line

463 or the mixing-controlled combustion layer is closer to the central region with higher P_{am}, which

464 increases the heat transfer. As shown in Fig. 13, the temperature in the rich premixed region

465 increases with P_{am}, contributing to the higher soot formation rates. Apart from these, it is noticed

466 that both the velocity near the spray region and χ decrease with the rise of P_{am}. This indicates the

467 mixing rate within the fuel-rich region decreases, promoting soot precursor and particle formation

468 within the fuel-rich region. These collectively contribute to the higher local $f_{v,soot}$ when P_{am}

469 increases.

470

471
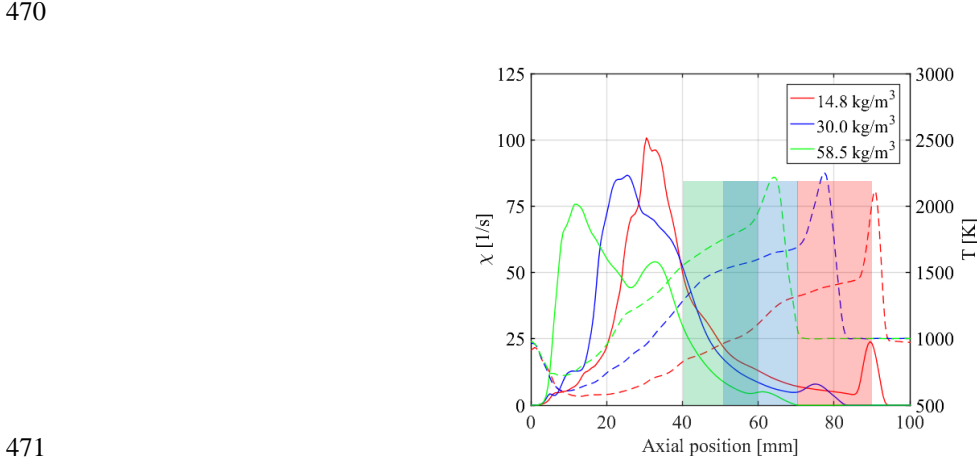
472 Fig. 13. Scalar dissipation rate, χ (solid lines) and temperature (dashed lines) along the spray axis.

473 Semi-transparent windows indicate the domains with high soot volume fraction as can be seen in

474 Figs. 7 to 9.

475

476 **Concluding remarks**

477 The contribution of this study is the generalization of the ignition behaviors and flame structures

478 at different ambient pressures (P_{am}) under diesel engine-like conditions. Diesel #2 spray flames at

479 three P_{am} levels of 42, 85 and 170 bar have been studied using an Eulerian-based transported

480 probability density function model in three-dimensional computational fluid dynamic

481 simulations. Comparisons to measurements show that the ignition delay times and flame lift-off

482 lengths are predicted fairly well. The numerical results show that the mixture fraction of the first

483 igniting mixture during the high-temperature ignition does not vary monotonically with P_{am}. The

484 high-temperature ignition takes place on the fuel-rich side in the 42 bar and 85 bar cases.

485 However, at 170 bar the high-temperature ignition occurs on the fuel-lean side due to the

22

increased reaction rates and temperature in the fuel-lean mixture. The main ignition in all three cases occurs in the region where the scalar dissipation rate (χ) is low and the residence time is long. Analyses of the quasi-steady spray flame structures reveal that the stoichiometric mixtures are closer to the fuel-rich core when P_{am} is increased, leading to higher heat transfer and increased temperature within the fuel-rich core. Besides that, χ reduces in cases with higher P_{am}. These collectively contribute to the higher local soot volume fraction when P_{am} increases, in addition to poorer air entrainment attributed by the reduced lift-off length and the increased reaction rates.

Acknowledgements

References

1. Hult J, Matlok S, Mayer S. Particle image velocimetry measurements of swirl and scavenging in a large marine two-stroke diesel engine. SAE paper 2014;2014-01-1173.

2. Hult J, Matlok S, Mayer S. Optical diagnostics of fuel injection and ignition in a marine two-stroke diesel engine. SAE Int J Engine 2014;7:2014-01-1448.

3. Engine Combustion Department of Sandia National Laboratories. Engine Combustion Network. Available at < http://www.sandia.gov/ecn/ > [Accessed on 17 December 2017]

4. Krisman A, Hawkes ER, Talei M, Bhagatwalaa A, Chen JH. A direct numerical simulation of cool-flame affected autoignition in diesel engine-relevant conditions. Proc Combust Inst 2017;36:3567-75.

5. Dahms RN, Paczko GA, Skeen SA, Pickett LM. Understanding the ignition mechanism of high-pressure spray flames. Proc Combust Inst 2017; 36:2615-23.

512   6.   Kundu P, Ameen MM, Som S. Importance of turbulence-chemistry interactions at low

513   temperature engine conditions. Combust Flame 2017;183:283-98.

514   7.   Pei Y, Hawkes ER, Bolla M, Kook S, Goldin GM, Yang Y, Pope SB, Som S. An analysis

515   of the structure of an *n*-dodecane spray flame using TPDF modelling. Combust Flame

516   2016;168:420-35.

517   8.   Siebers DL. Scaling liquid-phase fuel penetration in diesel sprays based on mixing-limited

518   vaporization. SAE Paper 1999;1999-01-0528.

519   9.   Naber JD, Siebers DL. Effects of gas density and vaporization on penetration and

520   dispersion of diesel sprays. SAE Paper 1996;960034.

521   10.   Siebers D, Higgins B. Flame lift-off on direct-injection diesel sprays under quiescent

522   conditions. SAE Paper 2001;2001-01-0531.

523   11.   Pickett LM, Siebers DL. Orifice diameter effects on diesel fuel jet flame structure. J Eng

524   Gas Turbines Power 2005;127:187-96.

525   12.   Higgins B, Siebers D, Aradi A. Diesel-spray ignition and premixed-burn behavior. SAE

526   Paper 2000:2000-01-0940.

527   13.   Pickett LM, Siebers DL. Soot in diesel fuel jets: effects of ambient temperature, ambient

528   density, and injection pressure. Combust Flame 2004;138:114-35.

529   14.   Pang KM, Karvounis N, Walther JH, Schramm J. Numerical investigation of soot

530   formation and oxidation processes under large two-stroke marine diesel engine-like

531   conditions using integrated CFD-chemical kinetics. Appl Energy 2016;169:874-87.

532   15.   Pang KM, Karvounis N, Walther JH, Schramm J, Glarborg P, Mayer S. Modelling of

533   temporal and spatial evolution of sulphur oxides and sulphuric acid under large, two-stroke

534   marine engine-like conditions using integrated CFD-chemical kinetics. Appl Energy

535   2017;193:60-73.

536   16.   Som S, Aggarwal SK. Effects of primary breakup modeling on spray and combustion

537   characteristics of compression ignition engines. Combust Flame 2010;157:1179-93.

538   17.   Bolla M, Gudmundsson T, Wright YM, Boulouchos K. Simulations of diesel sprays using

539   the Conditional Moment Closure model. SAE Int J Engine 2013;6:1249-61.

540   18.   Valino L. A field Monte Carlo formulation for calculating the Probability Density Function

541   of a single scalar in a turbulent flow. Flow, Turb Combust 1998;60:157-72.

542   19.   Liu S, Hewson JC, Chen JH, Pitsch H. Effects of strain rate on high-pressure nonpremixed

543   n-heptane autoignition in counterflow. Combust Flame 2004;137:320-39.

544   20.   Pang KM, Jangi M, Bai X-S, Schramm J. Evaluation and optimisation of

545   phenomenological multi-step soot model for spray combustion under diesel engine-like

546   operating conditions. Combust Theor Model 2015;19:279-308.

547   21.   Hashemi H, Christensen JM, Gersen S, Levinsky H, Klippenstein SJ, Glarborg P. High-

548   pressure oxidation of methane. Combust Flame 2016;172:349-64.

549   22.   Hashemi H, Jacobsen JG, Rasmussen CT, Christensen JM, Glarborg P, Gersen S, Essen M,

550   Levinsky H, Klippenstein SJ. High-pressure oxidation of ethane. Combust Flame

551   2017;182:155-60.

552   23.   Hashemi H, Christensen JM, Harding LB, Klippenstein SJ, Glarborg P. High-pressure

553   oxidation of propane. Proc Combust Inst 2018; https://doi.org/10.1016/j.proci.2018.07.009.

554   24.   Mehl M, Pitz WJ, Westbrook CK, Curran HJ. Kinetic modeling of gasoline surrogate

555   components and mixtures under engine conditions. Proc Combust Inst 2011;193-200.

556   25.   Lu T, Law CK. Strategies for mechanism reduction for large hydrocarbon: n-heptane.

557   Combust Flame 2008;154:153-63.

558   26.   Zhang K, Banyon C, Bugler J, Curran HJ, Rodriguez A, Herbinet O, Battin-Leclerc F,

559   B'Chir C, Heufer KA. An updated experimental and kinetic modeling study of n-heptane

560   oxidation. Combust Flame 2016;172:116-35.

561   27.   Pei Y, Liu W, Mehl M, Som S, Lu T, Pitz WJ. A multicomponent blend as a diesel fuel

562   surrogate for compression ignition engine applications. J Eng Gas Turbines Power

563   2005;137:Paper GTP-15-1057.

564   28.   Poon HM, Pang KM, Ng HK, Gan S, Schramm J. Development of multi-component diesel
565   surrogate fuel models. Part II: validation of the integrated mechanisms in 0-D kinetic and 2-
566   D CFD spray combustion simulations. Fuel 181;2016:120–30.

567   29.   Anon. CHEMKIN-PRO software: Theory manual. Reaction Design 2008.

568   30.   Mastorakos E, Baritaud TA, Poinsot TJ. Numerical simulations of autoignition in turbulent
569   mixing flows. Combust Flame 1997;109:198-223.

570   31.   Mastorakos E. Ignition of turbulent non-premixed flames. Prog Energy Combust Sci 2011;
571   35:57-97.

572   32.   Pei Y, Hawkes ER, Kook S. A comprehensive study of effects of mixing and chemical
573   kinetic models on predictions of n-heptane jet ignitions with the PDF method. Flow, Turbul
574   Combust 2013;91:249-80.

575   33.   The OpenFOAM Foundation. 2015. Available at < www.openfoam.org/ > [Accessed on 8
576   September 2016]

577   34.   Easley W, Mellor A. NO Decomposition in Diesel Engines. SAE Paper 1999;1999-01-
578   3546.

579   35.   Pang KM, Jangi M, Bai X-S, Schramm J, Walther JH. Modelling of ignition and flame
580   liftoff using an accelerated Eulerian Stochastic Fields method. Combust Flame
581   2018;193C;363-83.

582   36.   Jangi M, Lucchini T, Gong C, Bai X-S. Effects of fuel cetane number on the structure of
583   diesel spray combustion: An accelerated Eulerian stochastic fields method. Combust Theor
584   Model 2015;19:549-67.

585   37.   Bolla M, Chishty MA, Hawkes ER, Chan NQ, Kook S. Influence of turbulent fluctuations
586   on radiation heat transfer, NO and soot formation under ECN Spray A conditions. Proc
587   Combust Inst 36;2017:3551-8.

588   38.   Gordon RL, Masri AR, Pope SB, Goldin GM. Transport budgets in turbulent lifted flames
589   of methane autoigniting in a vitiated co-flow. Combust Flame 2007;151:495-511.

590   39.   Mizobuchi Y, Tachibana S, Shinio J, Ogawa S, Takeno T. A numerical analysis of the

591   structure of a turbulent hydrogen jet lifted flame. Proc Combust Inst 2002;29:2009-15.

592   40.   Dec JE. A conceptual model of DI diesel combustion based on laser-sheet imaging. SAE

593   Paper 1997:970873.

594   41.   Flynn PF, Durrett RP, Hunter GL, zur Loye AO, Akinyemi OC, Dec JE, Westbrook CK.

595   Diesel combustion: An integrated view combining laser diagnostics, chemical kinetics, and

596   empirical validation. SAE Transactions 108;1999:587-600.